Lu *et al. Biochar* (2024) 6:35
https://doi.org/10.1007/s42773-024-00325-2

Biochar

ORIGINAL RESEARCH Open Access

Synthesis of invasive plant biochar catalyst with carbon nitride structure for peroxymonosulfate activation toward efficient ciprofloxacin degradation

Yu-Wei Lu[1,2,3], Yu-Han Fan[1,3] and Ming Chen[1,3*]

Abstract

In this work, an invasive plant (*Aster subulatus Michx*) mesopore laminar biochar loaded with transition metal Co (CoS@MLBC) was synthesized by a one-step hydrothermal carbonization way for activating peroxymonosulfate (PMS) to remove antibiotics in water. We characterized the structure and morphology of CoS@MLBC and tested its performance. The results showed that the carbon nitride structure was formed on CoS@MLBC, which improved its adsorption capacity for antibiotics and PMS. In addition, Co-doping significantly enhanced the PMS activity and efficiently degraded ciprofloxacin (CIP) over a wide pH range. It was identified that radical and non-radical synergistic action had a critical effect on the CIP degradation process. Furthermore, CoS@MLBC could completely remove CIP within 10 min and had a high removal efficiency (98%) after four cycles. Three possible pathways of the CIP degradation process with 12 intermediates were proposed and their ecotoxicity was analyzed. This work provides a new perspective for preparing biochar from invasive plants for the degradation of antibiotics in water, realizing the concept of "treating the wastes with wastes".

Highlights

- A novel catalyst CoS@MLBC with the carbon nitride structure was synthesized.
- •OH, SO_4•$^-$ and $^1O_2$ were the main active species in the ciprofloxacin degradation process.
- Twelve intermediates were qualitatively determined and identified.

Keywords Invasive plant-derived biochar, Carbon nitride structure, Peroxymonosulfate

Handling editor: Xing Yang

*Correspondence:
Ming Chen
chenming@cigit.ac.cn; mchensn@hnu.edu.cn
Full list of author information is available at the end of the article

Springer

Graphical Abstract

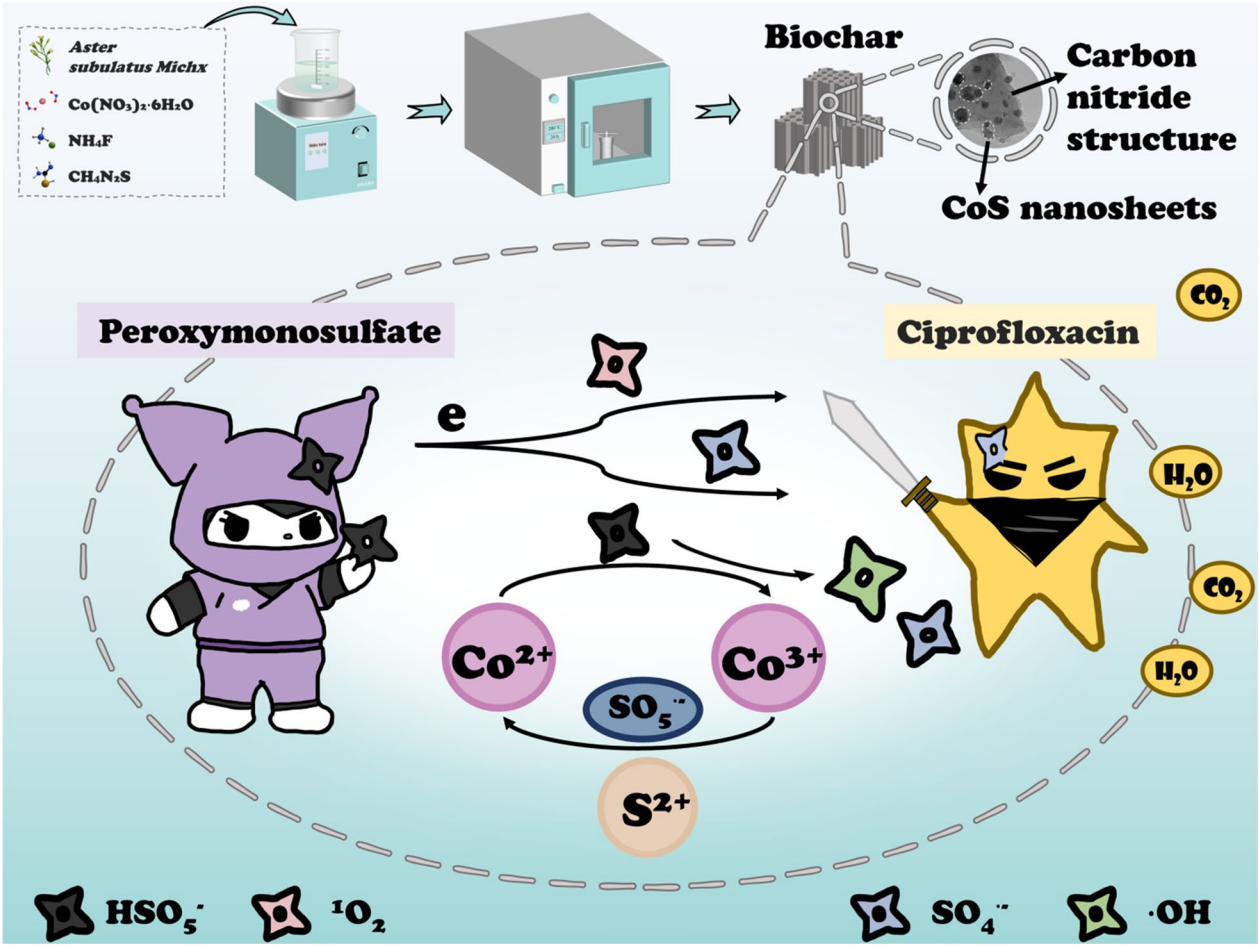

1 Introduction

Water pollution by antibiotics has become a global environmental problem due to incomplete metabolism in humans or animals, unsatisfactory removal by conventional processes, and unintentional wastewater discharges from pharmaceutical plants and hospitals (Li et al. 2018, 2024; Liu et al. 2023a). Traditional wastewater treatment technologies, such as adsorption, flocculation, biotechnology, and membrane technology, fail to completely remove antibiotics from the environment (Rodriguez-Narvaez et al. 2017). Therefore, developing cost-effective approaches to remediate antibiotic-contaminated water is an important goal. Advanced oxidation processes (AOPs) have received increasing attention in recent studies (Zhang et al. 2020; Sun et al. 2020; Wang et al. 2023a). Compared to hydroxyl radicals, sulfate radicals have higher redox potentials, longer half-life, higher oxidation selectivity, and broader applicability, which ensure efficient electron transfer and binding to target contaminants (Andrew Lin et al. 2015; Mei et al. 2019; Chen et al. 2015). The oxidizing agents commonly used to produce sulfate radicals are peroxymonosulfate (PMS) and peroxydisulfate (PDS), and PMS is more accessible to be activated than PDS (Nguyen et al. 2022). Moreover, transition metal catalysts can effectively activate PMS. Compared to Fe, Mn, and Cu, Co-based catalysts exhibit better performance in PMS activation (Cao et al. 2020a; Nguyen et al. 2021). However, the aggregation and ion leaching in the water of Co-based catalysts restrict their large-scale application.

Biochar is a sustainable resource known for its effectiveness as an adsorbent due to its porous structure, significant surface area, functional groups, large cation exchange capacity, and efficient removal of pollutants

(Ren et al. 2023; Liu et al. 2024; Jiang et al. 2024). However, many studies have demonstrated that the oxygenated functional groups in pure biochar restrict its adsorption ability for antibiotics (Liang et al. 2023a; Liao et al. 2022). Furthermore, the restricted pores and specific surface area of pure biochar also restrict its ability to absorb antibiotics (Huang et al. 2021). Thus, recent studies on removing antibiotics from water have used biochar as catalysts for the AOPs. It has been demonstrated that biochar can remove organic pollutants from water (Lei et al. 2022; Liu et al. 2023b; Jiang and Dai 2023). Recently, g–C_3N_4 was researched as an effective catalyst due to its high catalytic activity, non-toxicity, and physical and chemical stability (Bicalho et al. 2020; Chen et al. 2021). Liang et al. (Liang et al. 2023b) prepared hollow Co_3O_4 confined in carbon nitride (CN) through in situ growth, and the results showed that the catalyst has good hydrophilicity and efficiently degrades CIP. Zhao et al. (Zhao et al. 2022) synthesized a single atom with CN structure, which effectively promotes the production of $^1O_2$ and efficiently degrades sulfamethoxazole. However, these methods often require high temperatures and tedious synthesis processes, which are time-consuming and energy-wasting.

Hydrothermal carbonization (HTC) uses renewable biomass resources as precursors and aqueous solutions as reaction solvents and undergoes a series of combined chemical reactions, such as dehydration and decarboxylation (Byambaa et al. 2023). HTC could convert biomass into a carbon-rich solid phase called hydrochar or biochar at a temperature of 180–250 °C and 10–50 bar pressures, and the energy consumption is lower than pyrolysis (Nguyen et al. 2023). The biochar obtained from HTC showed higher adsorption capacity, and the biochar had less ash content and a more dispersed structure (Krysanova et al. 2019). Furthermore, the yield of biochar obtained from HTC could be achieved at 67.94% and is easily biodegradable (Sengottian et al. 2022). Therefore, HTC has become a cost-effective process that produces hydrochar with desirable properties.

Most previous studies chose woody and gramineous plants as biomass, but these plants' high cellulose content and stable structure are difficult to hydrolyze in common solvents and at low temperatures (Sun et al. 2022). Therefore, many studies have utilized HTC and pyrolysis together to create biochar. However, this approach has complicated the preparation process (Kuan et al. 2022; Bopda et al. 2022). In general, herbaceous plants possess a greater amount of lignin as compared to woody plants. Given their high carbon and low oxygen content, they are an exceptional source material for biochar. Furthermore, the multifaceted nature of lignin, characterized by aromatic rings, methoxyl, carboxyl, and hydroxy groups, renders them even more fitting for the creation of biochar substances (Sun et al. 2022).

Invasive plants are defined as non-native plants that grow in the wild and have rapidly growing populations (Pyšek et al. 2004; Essl et al. 2018). The human-mediated action has greatly accelerated the invasion of non-native plants by helping species spread over biogeographic barriers and overcome environmental and reproductive barriers (Pyšek and Richardson 2010). Synergies between biological invasions and other drivers of ecosystem degradation exacerbate current invasions and increase their scope and impacts (Pyšek et al. 2020). Once invasive plants become dominant, they can displace native vegetation and disrupt the original ecosystem (Zhou et al. 2023). In recent years, some researchers have demonstrated that invasive plant species can also be used to prepare biochar to remove pollutants from water (Li et al. 2023; Wang et al. 2023b). Compared to traditional biomass (e.g., straw, corn cobs, and husks), invasive plant-derived biochar exhibits significant differences in structure, composition, and adsorption performance (Zhang et al. 2018; Feng et al. 2021). Specifically, invasive plants are diverse and widely distributed, making them ideal feedstocks for biochar production. Therefore, selecting invasive plants as raw biomass solves the environmental challenges and responds to the call for " treating the wastes with waste" technology. As far as our knowledge extends, no study has been reported using biochar obtained from the invasive plant *Aster subulatus Michx* (ASM).

In this study, we developed biochar using invasive plants by a one-step HTC method to remove antibiotics in water. Ciprofloxacin was used as the model contaminant. The structure and functional groups of the biochar were characterized. We evaluated the influence of solution pH and anions in water on the degradation process. Furthermore, the active species, degradation pathways and intermediates were identified. Finally, the toxicity prediction of CIP degradation intermediates was performed using EPI Suite software. This work found that the mesopore laminar biochar loaded with transition metal Co (CoS@MLBC) catalyst had excellent CIP degradation performance, increasing the potential for invasive plant applications in PMS activation on wastewater treatment. The results provide new perspectives for synthesizing simple and environmentally friendly catalysts.

2 Experimental section

2.1 Materials

The details of chemicals and invasive plants are described in Additional file 1: Text S1.

ASM was collected from the water level fluctuation zone in Three Gorges Reservoir, and the samples were washed and dried in an oven at 60 °C for 24 h until they

reached a constant weight. After grinding, they were sieved with a 100-mesh sieve and stored in a dry environment pending further experiments. The real water was collected from the slow-gathering area, Zhuxi River. The sampling process and site information are presented in Additional file 1: Text S1 and Table S1.

2.2 Preparation of CoS@MLBC

The CoS@MLBC catalyst was synthesized by the facile one-step HTC method, as depicted in Scheme 1. First, 0.87 g Co $(NO_3)_2{\cdot}6H_2O$, 0.33 g NH_4F, 1.02 g CH_4N_2S, and 1 g ASM were added into 100-mL ultrapure water and kept stirring for 18 h at room temperature. The mixture was then poured into a 200 mL autoclave and heated at 200 °C for 24 h. After the autoclave was cooled to room temperature, the obtained catalysts were collected by centrifugation. Catalysts were thoroughly rinsed with ethanol and water to remove impurities, then dried at 60 °C and stored under dry and light-proof conditions for subsequent experiments. At the same time, the pure ASM biochar (BC), the pure cobalt metal (CoS), and other biomass catalysts Co-Corn, and Co-WS were synthesized for comparison, and the preparation process is described in detail in Additional file 1: Text S2.

2.3 Characterization

The CoS@MLBC was characterized by scanning electron microscopy (SEM), high-resolution transmission electron microscopy (HRTEM) for structural observation, powder X-ray diffraction (XRD) to determine the catalyst phase composition, X-ray photoelectron spectroscopy (XPS) for chemical compositional analysis, Fourier transform infrared spectroscopy (FTIR) to analyze the surface functional groups, electron paramagnetic resonance (EPR) for identification of the active species, and Bruno-Emmett-Taylor (BET). Cyclic voltammetry (CV) and electrochemical impedance spectroscopy (EIS) were used to analyze the electron transfer at the catalyst surface. The characterizations and instrument parameters for the catalyst samples are detailed in Additional file 1: Text S3.

2.4 Experimental procedure

The CIP degradation experiments were conducted under magnetic stirring conditions at room temperature. Briefly, 50 mL of CIP solution (10 mg L^{-1}) and a determined amount of catalyst were added to a 100 mL beaker and stirred for 30 min to achieve adsorption equilibrium. After adding PMS, a 2.5 mL sample aliquot was collected at 1 min, 2 min, 5 min, 10 min,

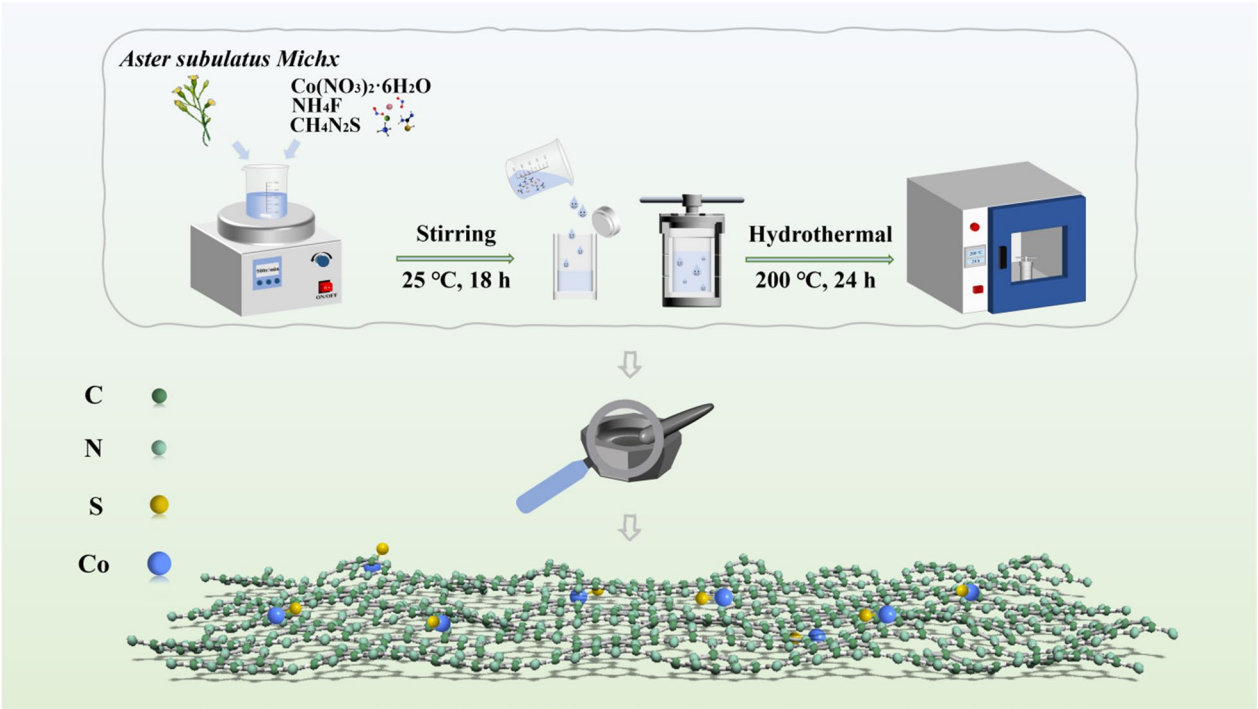

Scheme 1. Schematic demonstration for the synthetic procedure of CoS@MLBC

15 min, 20 min, respectively, and promptly quenched with 0.5 mL methanol. Subsequently, the resulting solution was filtered through a 0.22 μm injection filter and transferred for UV–vis and HPLC–MS analysis. And the CIP intermediates were analyzed by HPLC–MS. The leaching of cobalt was quantified using inductively coupled plasma mass spectrometry (ICP-MS). Additionally, the impact of catalyst and PMS dosage was investigated. The stability of the catalyst was determined by adjusting the initial pH, the anionic species, and application experiments in real aqueous environments. The recyclability of the catalyst was investigated through four-cycle tests. The recovered material was rinsed, dried, and recycled for three more cycles under the same experimental conditions. The experiments in this study were conducted in triplicate, and the mean values were utilized for statistical analysis.

2.5 Toxicity test

The Estimation Program Interface (EPI Suite) was used to assess acute and chronic toxicity levels of CIP and its degradation products on marine organisms spanning three trophic levels. The potential ecotoxicity of the CoS@MLBC was evaluated by employing a *Vigna radiata* growth test. The growth of *Vigna radiata* can reflect the potential ecological risk of the water. The description of the culture conditions, pretreatment and toxicity tests for *Vigna radiata* is presented in Additional file 1: Text S4.

3 Results and discussion

3.1 Characterization of CoS@MLBC catalyst

SEM and TEM imaging (Fig. 1) showed the surface morphology of as-obtained synthesized catalysts. The SEM images showed (Fig. 1a, b) that CoS@MLBC exhibited a porous lamellar structure, and many raised particles were observed on the surface. Tan et al. (Tan et al. 2019) reported that sulfur species could loosen the structure and form a pore-like structure during the synthesis of S-doped materials. Figure 1d, e show the TEM and HRTEM images of CoS@MLBC. The (100) crystal plane of CoS could be observed from the HRTEM image, as shown in Fig. 1e, f. In addition, the Energy Dispersive Spectrometer (EDS, Additional file 1: Fig. S1a) illustrated the elemental composition of CoS@MLBC. The elemental mapping image (Fig. 1c) further confirmed the homogeneous distribution of C, N, O, Co, and S species within the catalyst. Additionally, Additional file 1: Fig. S2

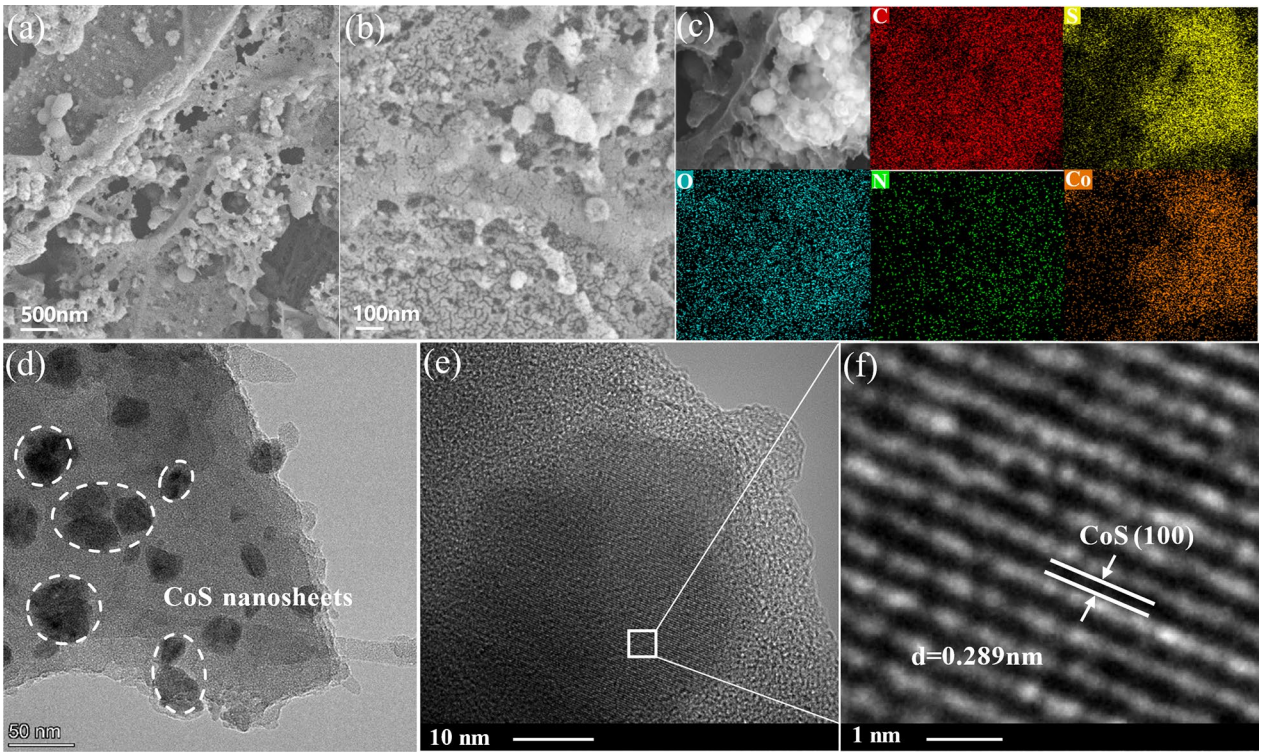

Fig. 1 SEM images of CoS@MLBC (**a**), (**b**), EDX elemental mapping of CoS@MLBC (**c**), TEM image of CoS@MLBC (**d**), and HRTEM imagines of CoS@MLBC (**e**), (**f**)

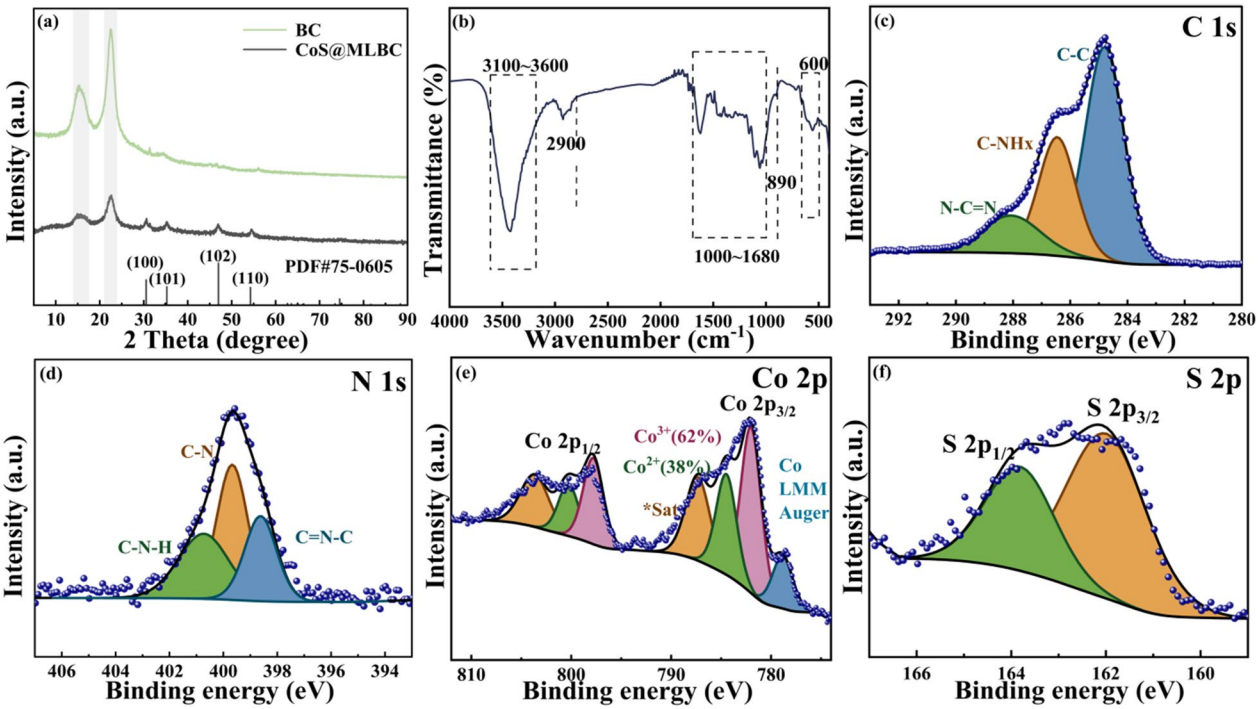

Fig. 2 The XRD pattern of the prepared catalysts (**a**), FTIR image (**b**), and XPS spectra of CoS@MLBC: C 1s (**c**), N 1 s (**d**), Co 2p (**e**), S 2p (**f**)

presents the N_2 adsorption–desorption isotherms data, elucidating the pore size distribution. In accordance with the IUPAC classification, the CoS@MLBC isotherm conformed to a type IV isotherm exhibiting an H3 hysteresis loop, indicative of a mesoporous structure.

The XRD pattern of CoS@MLBC is depicted in Fig. 2a, revealing distinct diffraction peaks at $2\theta = 30.56°$, 35.26°, 46.98°, and 54.28° match the (100), (101), (102), and (110) crystal planes, respectively, of CoS (PDF#75–0605). This analysis result was consistent with that of HRTEM. Furthermore, the diffraction peaks at 15.1° and 22.5° match the (001) and (100) crystal planes of g-C_3N_4(PDF#87-1526), respectively, indicating the synthesis of carbon nitride structure. The XRD pattern of BC indicated that the catalyst also formed the structure of CN (Fig. 2a). Compared with BC, the (001) and (100) peaks of CoS@MLBC were further weakened, indicating that the metal successfully combined with BC under the condition that did not change the structure of CN. As shown in Additional file 1: Fig. S3a, the distinct diffraction peaks of pure Co catalyst evidenced the synthesis of CoS crystal. In summary, the XRD patterns illustrated that the carbon nitride structure was successfully synthesized using a one-step HTC method based on ASM as biomass.

The FTIR spectra also revealed similar observations (Fig. 2b). The peaks observed at the range of $1000 \sim 1680\ cm^{-1}$ in the two curves can be attributed to the stretching vibration of the C–N and C=N–C heterocyclic skeletons (Bharathi et al. 2023; Shaheen et al. 2022; Yu et al. 2023). And the peak at 890 cm^{-1} corresponds to the bending vibration of tri-s-triazine rings (Wang et al. 2019). Moreover, the peak observed at 600 cm^{-1} and 1100 cm^{-1} can be ascribed to the surface oxidation of sulfur species on the catalyst and the presence of Co-S bonds, respectively (Mahmoud et al. 2021; Yuan et al. 2020). The stretching vibrations of $-CH_3$, $-CH_2-$ appeared at 2900 cm^{-1}. A broad peak between 3100 and 3600 cm^{-1} is due to the N–H and O–H stretching modes, which can be attributed to the N–H groups on the uncondensed surfaces and the absorbed H_2O (Qiu et al. 2024; Wen et al. 2023).

XPS was used to analyze the change of elemental composition and valence states on the catalyst surface. The full XPS survey scan spectrum indicated that CoS@MLBC was comprised of C, O, N, S, and Co elements (Additional file 1: Fig. S4a). Figure 2c–f shows the high-resolution spectra of C 1 s, N 1 s, Co 2p, and S 2p peaks in CoS@MLBC. The C 1 s spectra of CoS@MLBC (Fig. 2c) could be deconvoluted into three distinct peaks at 284.8 eV, 286.5 eV, and 288.5 eV, which correspond to adventitious carbon (C–C bond), C-NH_x and sp^2-bonded carbon (N–C=N), respectively (Qiu et al. 2024; Balakrishnan et al. 2023; Liu et al. 2021). Figure 2d displays

the three peaks at 398.62 eV, 399.68 eV and 400.73 eV were attributed to C=N–C, C–N, and C–N–H, respectively (Peng et al. 2021). The four peaks at 782.00 eV, 784.47 eV, 797.77 eV, and 800.26 eV can be ascribed to $Co^{3+}2p_{3/2}$, $Co^{2+}2p_{3/2}$, $Co^{3+}2p_{1/2}$, $Co^{2+}2p_{1/2}$, respectively (Fig. 2e). The percentage of Co^{2+} and Co^{3+} were about 38% and 62%, respectively, and Co^{3+} was considered to be the surface oxidation of CoS (Fang et al. 2022). As shown in Fig. 2f, the two distinct peaks at 162.18 eV and 164.31 eV can be attributed to the S $2p_{3/2}$ and S $2p_{1/2}$, respectively.

3.2 Performance analysis

3.2.1 Catalyst comparison

The CIP was selected as the model antibiotic and the removal efficiencies of CIP by CoS@MLBC/PMS, Co/PMS, BC/PMS, and PMS systems were 100%, 98.13%, 17.01%, and 7.68%, respectively, within 10 min (Fig. 3a). The reaction rate constants (k_{obs}) of CoS@MLBC/PMS, Co/PMS, BC/PMS and PMS systems were 0.6865, 0.3570, 0.0062, and 0.0053 min^{-1}, respectively (Additional file 1: Fig. S5a). The control tests showed that CIP was relatively stable in the catalyst-free PMS system. The results indicate that the oxidant cannot decompose CIP alone. Compared with that of BC/PMS, the CoS@MLBC/PMS system showed an obvious superiority in CIP removal; the k_{obs} of CoS@MLBC/PMS showed an almost 110-fold increase (k_{obs} increased from 0.0062 min^{-1} to 0.6865 min^{-1}). And according to the contact angle analysis (Additional file 1: Fig. S6), the Co-doped enhanced the hydrophilicity of catalysts, which indicated that metal ions played a critical role in PMS activation. Apparently, CoS@MLBC had better performance than CoS,

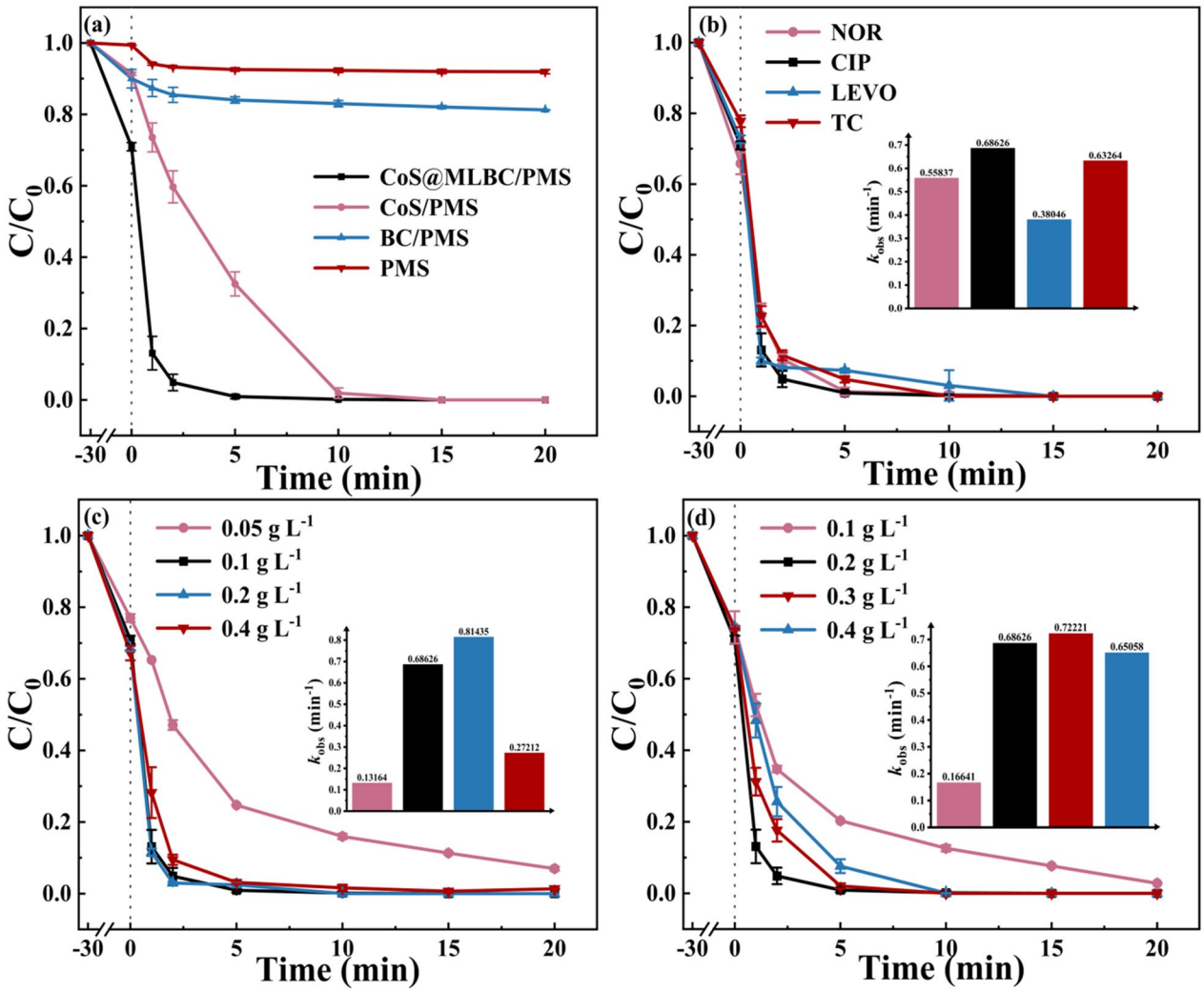

Fig. 3 Removal efficiency of CIP by different systems (**a**), different antibiotics (**b**), and effect of catalyst dosage (**c**), PMS dosage (**d**). Conditions: $[CIP]_0 = 10$ mg L^{-1}, [Cata.] = 0.1 g L^{-1}, $[PMS]_0 = 0.2$ g L^{-1}, $pH_{ini} = 7.0$, T = 25 ℃

indicating that the hydrophilic structure of CN loaded in biochar enhanced the adsorption of the catalyst and improved catalytic performance.

According to the XRD patterns analysis of Co-Corn and Co-WS (Additional file 1: Fig. S3b and c), it was observed that there were no characteristic peaks of g-C_3N_4. The results showed that the invasive plants ASM as biomass could be used to successfully synthesize the catalyst with CN structure using the one-step HTC method. Besides, the CIP adsorption efficiencies of Co-Corn and Co-WS were 21% and 22% in 30 min, respectively (Additional file 1: Fig. S7a) and the CIP degradation efficiencies were only 55% and 48% in 20 min, respectively (Additional file 1: Fig. S7b). It was further illustrated that the CN structure could effectively improve the catalytic performance of catalysts.

To test the generalizability of the CoS@MLBC/PMS system in removing antibiotics, NOR, CIP, Levo, and TC were selected as target pollutants. The removal efficiencies of NOR, CIP, Levo, and TC were 99%, 100%, 97%, and 100%, respectively (Fig. 3b), indicating that the CoS@MLBC/PMS system exhibited good degradation performance for the abovementioned antibiotics. TC was more susceptible to degradation probably because its molecular structure was susceptible to attack by radicals (Fan et al. 2023a). The molecular masses of NOR, CIP, and Levo were similar, resulting in comparable degradation outcomes. The CIP was chosen as the paradigmatic antibiotic for forthcoming experiments.

In this work, we carried out an application evaluation of the CoS@MLBC/PMS system for the removal of CIP in actual water. As shown in Additional file 1: Fig. S5c and d, the degradation efficiency of CIP was 92% within 10 min and it was completely degraded within 20 min. Compared to the control test, the k_{obs} of CIP in real water (0.2720 min^{-1}) was lower than that of the control test (0.6863 min^{-1}). The possible reason for this is that the organic matter and inorganic ions in the water column affect the degradation efficiency of CIP, which agrees with the study of Fan et al. (Fan et al. 2023b). In addition, the comparison of various monometallic catalysts for the activation of PMS to pollutant degradation is presented in Additional file 1: Table S2. The proposed CoS@MLBC catalysts had the simplest preparation method while guaranteeing a high degradation efficiency. The comparative results showed that the CoS@MLBC catalyst efficiently activated the PMS degradation of CIP.

3.2.2 Effect of catalyst and PMS dosage

The impact of catalyst concentration on CIP degradation is illustrated in Fig. 3c. The results demonstrated a positive correlation between catalyst concentration and the removal efficiency of CIP, with an increasing trend observed within the range of 0.05 g L^{-1} to 0.1 g L^{-1} and k_{obs} increased from 0.1316 min^{-1} to 0.6863 min^{-1}. The degradation efficiency of CIP exhibited a slight decrease as the catalyst dosage was increased from 0.1 g L^{-1} to 0.4 g L^{-1}. The enhancement of degradation efficiency could be attributed to increased active sites as the catalyst concentration increases. However, the excess catalyst will activate PMS to produce many radicals quickly, which will cause radical quenching and reduce the degradation efficiency (Hong et al. 2019). Therefore, the concentration of 0.1 g L^{-1} of the catalyst was chosen for forthcoming experiments.

The concentration of PMS also affected the CIP degradation efficiency (Fig. 3d). The increase in PMS dosage from 0.1 g L^{-1} to 0.2 g L^{-1} led to a significant enhancement of CIP degradation efficiency, as evidenced by the observed k_{obs} increasing from 0.1664 min^{-1} to 0.6865 min^{-1}. The possible reason is that an elevation in PMS concentration leads to increased production of radicals. The degradation efficiency of CIP remained relatively stable within the PMS concentration range of 0.2 g L^{-1} to 0.4 g L^{-1}. On one hand, the ability of the reaction site to adsorb PMS was limited. On the other hand, the excess radicals would react with one another, which forms other active species with lower oxidation potential, thus reducing the degradation efficiency (Eqs. 1–2) (Fan et al. 2023a). Therefore, the concentration of 0.2 g L^{-1} of PMS was chosen for forthcoming experiments.

$$SO_4^{\cdot -} + SO_4^{\cdot -} \rightarrow S_2O_8^{2-} \quad (1)$$

$$SO_4^{\cdot -} + \cdot OH \rightarrow HSO_5^{-} \quad (2)$$

3.2.3 Effect of pH and anions

The impact of initial pH on the removal efficiency of CIP was detailed. The removal efficiency of CIP decreased from 100 to 94% (k_{obs} decreased from 0.6865 min^{-1} to 0.1992 min^{-1}) within 10 min when the initial pH was reduced from 7 to 3 (Fig. 4a). This might be due to the high H^+ concentration preventing the adsorption of PMS on the active sites, limiting its activation process (Long et al. 2021) (Eqs. 3–4). In addition, excessive H^+ inhibits the production of $CoOH^+$, which will scavenge hydroxyl radicals and sulfate radicals; thus, the degradation efficiency decreases under strong acid conditions (Eqs. 5–6). Furthermore, HSO_5^- and SO_5^{2-} are present at pH < 7.6, with HSO_5^- the dominant species and HSO_5^- more oxidizing and generating SO_4^- than SO_5^{2-} capacity (Cao et al. 2020b). Thus, the k_{obs} increased from 0.6865 min^{-1} to 0.8046 min^{-1} at pH = 5. At pH > 7.6, SO_5^{2-} was the dominant species, which reacts more readily with ·OH to generate $S_2O_8^{\cdot 2-}$ and further quench $SO_4^{\cdot -}$ (Eqs. 7–8). Therefore, the degradation efficiency of CIP was slightly

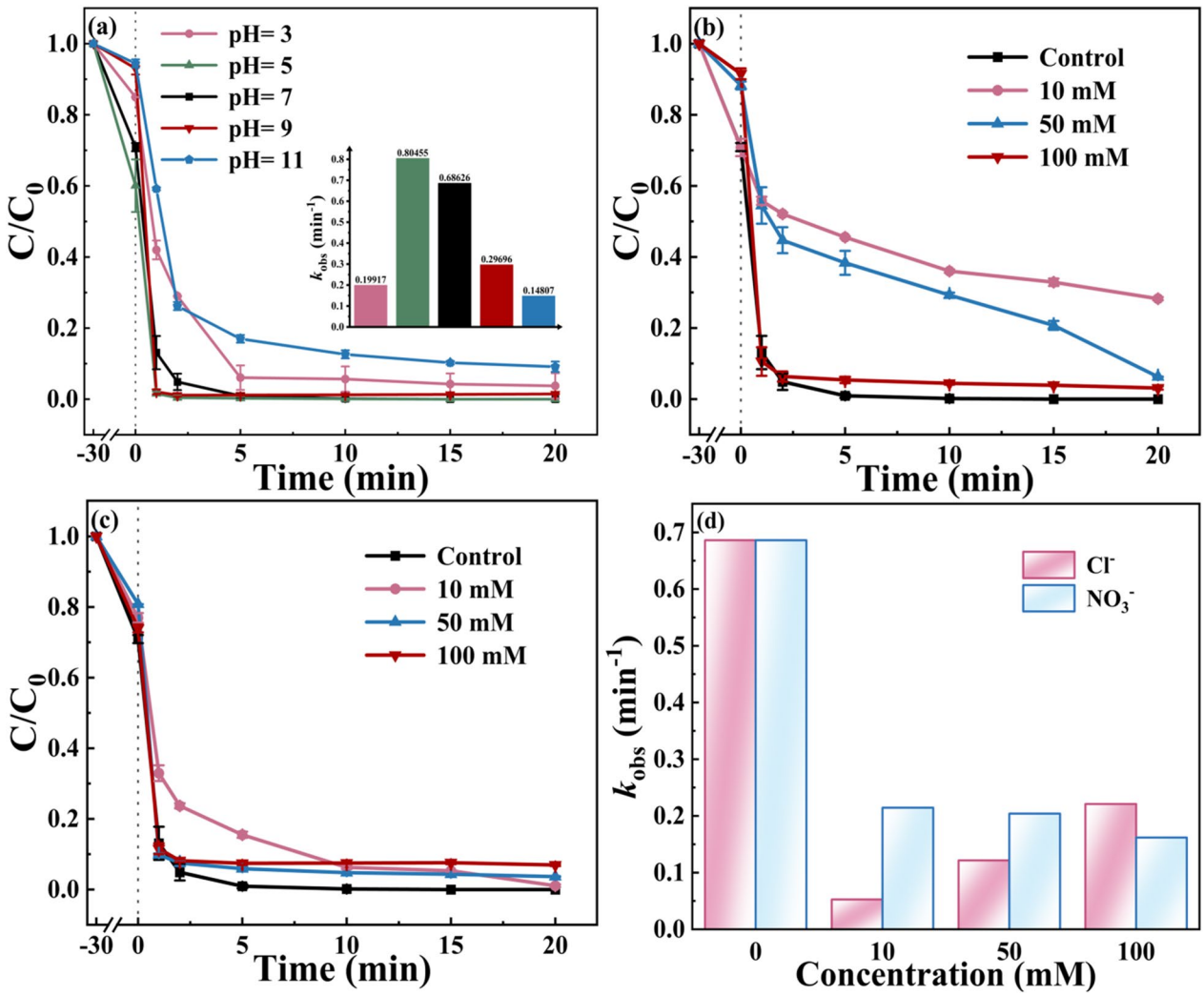

Fig. 4 Effect of pH (**a**), Cl^- (**b**), NO_3^- (**c**) and the k_{obs} of different concentrations of Cl^- and NO_3^- (**d**). Conditions: $[CIP]_0 = 10$ mg L^{-1}, [Cata.] = 0.1 g L^{-1}, $[PMS]_0 = 0.2$ g L^{-1}, $pH_{ini} = 7.0$, T = 25 ℃

inhibited under alkaline conditions. In conclusion, it is obvious that the removal efficiencies of CIP at pH = 3, 5, 7, 9, 11 were 96%, 100%, 100%, 98%, and 90%, respectively, indicating that CoS@MLBC/PMS maintained high efficiency in degrading CIP over a wide pH range.

$$H^+ + SO_4^{\cdot -} + e^- \rightarrow HSO_4^- \quad (3)$$

$$H^+ + \cdot OH + e^- \rightarrow H_2O \quad (4)$$

$$Co^{2+} + H_2O \rightarrow CoOH^+ + H^+ \quad (5)$$

$$CoOH^+ + HSO_5^- \rightarrow CoO^+ + H_2O + SO_4^- \quad (6)$$

$$\cdot OH + SO_5^{2-} \rightarrow S_2O_8^{\cdot 2-} \quad (7)$$

$$SO_4^{\cdot -} + S_2O_8^{\cdot 2-} \rightarrow S_2O_8^{\cdot -} + SO_4^{2-} \quad (8)$$

The effect of common ions (Cl^- and NO_3^-) in water on the CoS@MLBC/PMS system was investigated as shown in Fig. 4b, c. The inhibitory effect was significant when the Cl^- concentrations ranged from 10 to 50 mM, as depicted in Fig. 4b. At lower Cl^- concentrations, oxidation of Cl^- by $SO_4^{\cdot -}$ and ·OH leads to the formation of chlorides or hypochlorite ions (Wang et al. 2021), expressing the reaction (Eqs. 9–11). As shown in Fig. 4c, it could be observed that removal efficiency of 98%, 96%, and 93% corresponded to NO_3^- concentrations of

10 mM, 50 mM, and 100 mM, respectively. The results indicated that the presence of NO_3^- did not significantly impact the removal efficiency, but the reaction rate decreased with the increase in ion concentration. The decrease in CIP removal efficiency may be attributed to the reaction between external anions and ROSs, which form other active species, as demonstrated by the reaction in Eqs. 12–13.

$$Cl^- + \cdot OH \rightarrow HOCl^{\cdot -} \quad (9)$$

$$Cl^- + SO_4^{\cdot -} \rightarrow SO_4^{2-} + Cl\cdot \quad (10)$$

$$HOCl^{\cdot -} + H^+ \rightarrow Cl\cdot + H_2O \quad (11)$$

$$NO_3^- + SO_4^{\cdot -} \rightarrow SO_4^{2-} + NO_3\cdot \quad (12)$$

$$NO_3^- + \cdot OH \rightarrow OH^- + NO_3\cdot \quad (13)$$

3.2.4 Reusability and stability of CoS@MLBC/PMS system

The reusability of the CoS@MLBC/PMS system is a critical factor for practical applications. As presented in Additional file 1: Fig. S8a, the CoS@MLBC/PMS system showed no obvious loss of degradation efficiency over the 4 cycles and maintained its performance. After 20 min reaction, the removal efficiencies of CIP in 4 cycles were 100%, 100%, 99%, and 98%, respectively, and the k_{obs} is shown in Additional file 1: Fig. S8b. Furthermore, based on the XPS analysis of the catalyst before and after the reaction (Additional file 1: Fig. S4), no significant change was found in the Survey scan before and after use, and it is speculated that the decrease in CIP removal efficiency may be due to the change in the valence state of Co (Long et al. 2021b). In addition, carbonaceous catalysts are easily deactivated during PMS activation, which is a possible reason for the reduced CIP degradation efficiency (Yang et al. 2021). However, as shown in Additional file 1: Fig. S8c, the XRD patterns of the used catalysts did not exhibit any specific peaks, indicating no change in catalyst surface structure and composition. The findings suggest that the CoS@MLBC/PMS system exhibited a remarkable capability for efficient degradation of CIP and demonstrates excellent reusability. The FTIR spectra of fresh and used catalysts (Additional file 1: Fig. S8d) showed no significant change, further confirming the stability of CoS@MLBC. In addition, the CoS@MLBC/PMS system exhibited a lower leaching rate of Co ions than the Co/PMS system (Additional file 1: Fig. S5b). The results indicate that the biochar structure effectively immobilized Co ions and reduced ion leaching. The relevant calculations are given in Additional file 1: Text S5.

3.2.5 Toxicity test

In this work, we designed a *Vigna radiata* cultivation experiment to test the potential toxicity and ecological effects of CoS@MLBC. The control group (CG) was *Vigna radiata* cultivated with ultrapure water, and the treatment group (TG) was *Vigna radiata* cultivated with ultrapure water containing CoS@MLBC (the catalyst concentration of 0.1 g L^{-1}). According to Additional file 1: Fig. S10, the average stem length of CG was 20.52 cm, and the average root length was 10.86 cm. The mean stem length of TG was 20.97 cm and root length was 9.24 cm. The results for CG and TG were not significantly different, indicating that CoS@MLBC had no impact on the growth of *Vigna radiata*. In summary, CoS@MLBC is a simple and environmentally friendly catalyst.

3.3 Degradation mechanism

3.3.1 Identification of ROSs

The radical scavengers and EPR analysis were employed to identify the active species produced in the CoS@MLBC/PMS system. Tert-Butanol (TBA), methanol (MeOH), 1,4-Benzoquinone (pBQ) and NaN_3 were added in the CoS@MLBC/PMS system to quench ·OH, $SO_4^{\cdot -}$, $O_2^{\cdot -}$ and $^1O_2$, respectively. As shown in Fig. 5a, the addition of excess TBA significantly inhibited the degradation efficiency of CIP by 59%, providing evidence for the generation of ·OH in the CoS@MLBC/PMS system. Furthermore, adding MeOH inhibited 63% of CIP degradation, indicating that the contribution of $SO_4^{\cdot -}$ was also significant. Furthermore, NaN_3 inhibited CIP degradation by 55%, indicating that $^1O_2$ played a key role. In contrast, excess pBQ inhibited CIP degradation by 12%, indicating that $O_2^{\cdot -}$ may not be the primary active species. Overall, $O_2^{\cdot -}$ had little effect on the degradation of CIP, and ·OH, $SO_4^{\cdot -}$ and $^1O_2$ promoted the degradation of CIP. Based on the above analysis, the pathway of $O_2^{\cdot -}$, ·OH, $SO_4^{\cdot -}$ and $^1O_2$ production was explored. Firstly, HSO_5^- could self-decomposition to generate SO_5^{2-}, which react with ·OH to produce $HO_2^{\cdot -}$ (Additional file 1: Eqs. S3–5). And the $O_2^{\cdot -}$ was generated by the self-decomposition of $HO_2^{\cdot -}$, $SO_4^{\cdot -}$ and ·OH could be generated by the oxidation of Co^{2+} (Additional file 1: Eqs. S6-7), and HSO_5^- could gain electrons to produce $SO_4^{\cdot -}$ (Additional file 1: Eqs. S8). Besides, $SO_4^{\cdot -}$ could react with H_2O or OH^- to produce ·OH (Additional file 1: Eqs. S9-10). In addition, the CIP degradation under N_2 conditions was carried out, and the results showed that the effect of N_2 on CIP degradation was negligible (Additional file 1: Fig. S11), suggesting that $^1O_2$ was not formed by dissolved oxygen but by PMS activation. Furthermore, ·OH had a shorter lifespan than $^1O_2$, which might lead to its conversion to $^1O_2$ (Additional file 1: Eqs. S11). Therefore, $^1O_2$ might be

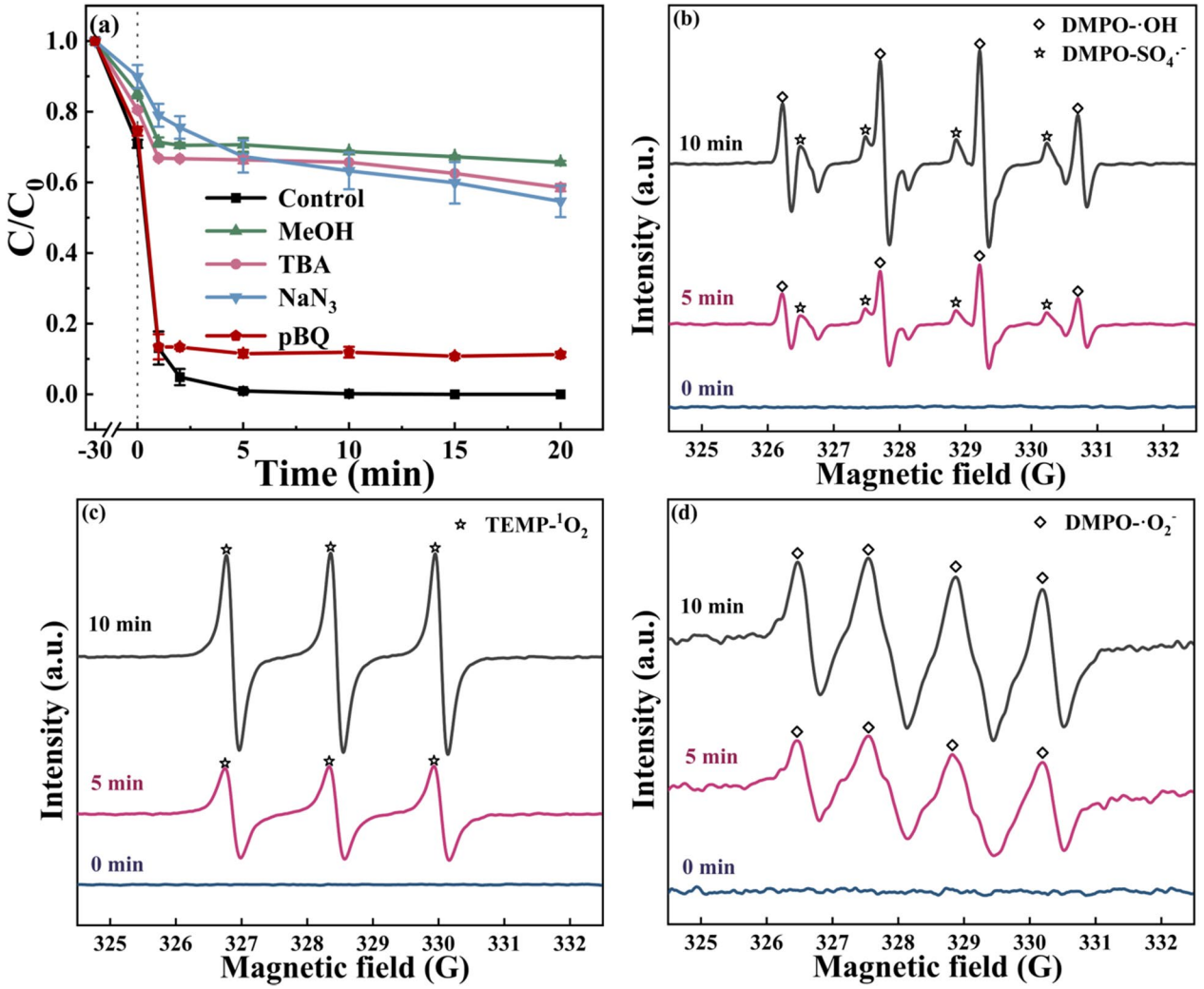

Fig. 5 Effect of radical scavengers on CIP removal in CoS@MLBC/PMS system (**a**), EPR spectra of •OH and $SO_4^{\cdot-}$ (**b**), $^1O_2$ (**c**), $O_2^{\cdot-}$ (**d**)

generated by the oxidation of PMS. In addition, Fig. 5b–d illustrates EPR analysis in the CoS@MLBC/PMS system, and the presence of •OH, $SO_4^{\cdot-}$, $^1O_2$ and $O_2^{\cdot-}$ was confirmed. The results were consistent with the quenching experiments.

3.3.2 The role of CoS and BC

According to Additional file 1: Fig. S4b, it is observed that the proportions of Co^{2+} decreased from 38 to 29%, and Co^{3+} increased from 62 to 71%. A part of Co^{2+} on the catalyst surface was oxidized to Co^{3+} during the activation of PMS. Fig. S4c illustrates that the S^{2-} proportion decreased from 65 to 58%, and the S_n^{2-} increased from 35 to 42%. Due to the low redox potential, S^{2-} was oxidized by PMS to expose Co^{2+}, which participates in the activation of PMS (Additional file 1: Eqs. S6-7). Previous studies have shown that the reaction of S^{2-} with PMS does not produce ROSs, but the low electronegativity of S^{2-} can promote the reduction of Co^{3+} to Co^{2+} (Additional file 1: Eqs. S12-13). The CoS/PMS could remove CIP to 100% in 20 min, while in the Co^{2+}/PMS system, the CIP removal efficiency was only 32% (Additional file 1: Fig. S12). This indicated that S^{2-} promotes the generation of Co^{2+} to activate PMS more effectively. For the mechanically mixed CoS and BC (1:1 mass ratio), the CIP removal was only 59%, which evidenced that chemical synthesis (CoS@MLBC) enhanced the binding of CoS and BC to improve the activation performance of PMS. The result indicates that BC could effectively enhance the electron transfer capacity of CoS to promote PMS decomposition in the CoS@MLBC/PMS system. The electrochemical analysis was performed to verify this conclusion. The cyclic voltammetry curve illustrated that CoS@MLBC had

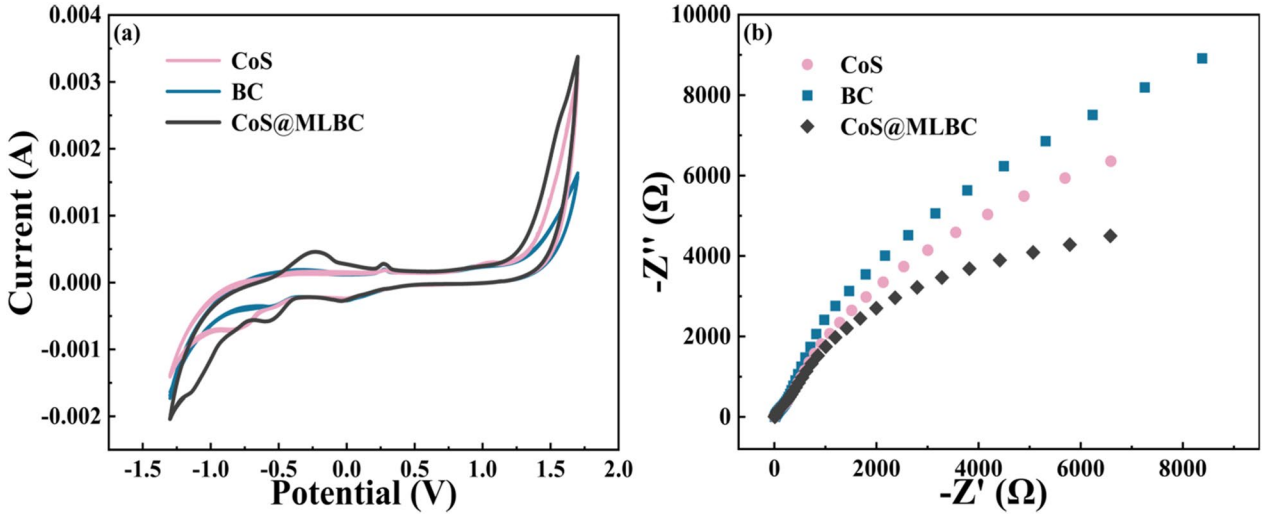

Fig. 6 Cyclic voltammetry curves (**a**) and EIS in 0.1 M Na_2SO_4 (**b**) of CoS, BC and CoS@MLBC

the highest current density compared to CoS and BC, indicating that CoS@MLBC had the highest reduction capacity (Fang et al. 2022) (Fig. 6a). The electron transfer potential of different catalyst surfaces was measured via electrochemical impedance spectroscopy (EIS). As shown in Fig. 6b, it could be observed that the arc radius of CoS@MLBC was smaller than that of CoS and BC, indicating that CoS@MLBC had lower impedance and higher electron transfer efficiency (Ren et al. 2019). Therefore, the combination of CoS and BC accelerated the electron transfer rate, and the carbon nitride structure improved the electron transfer performance of the catalysts in PMS activation, which was consistent with the results of previous studies (Shang et al. 2019).

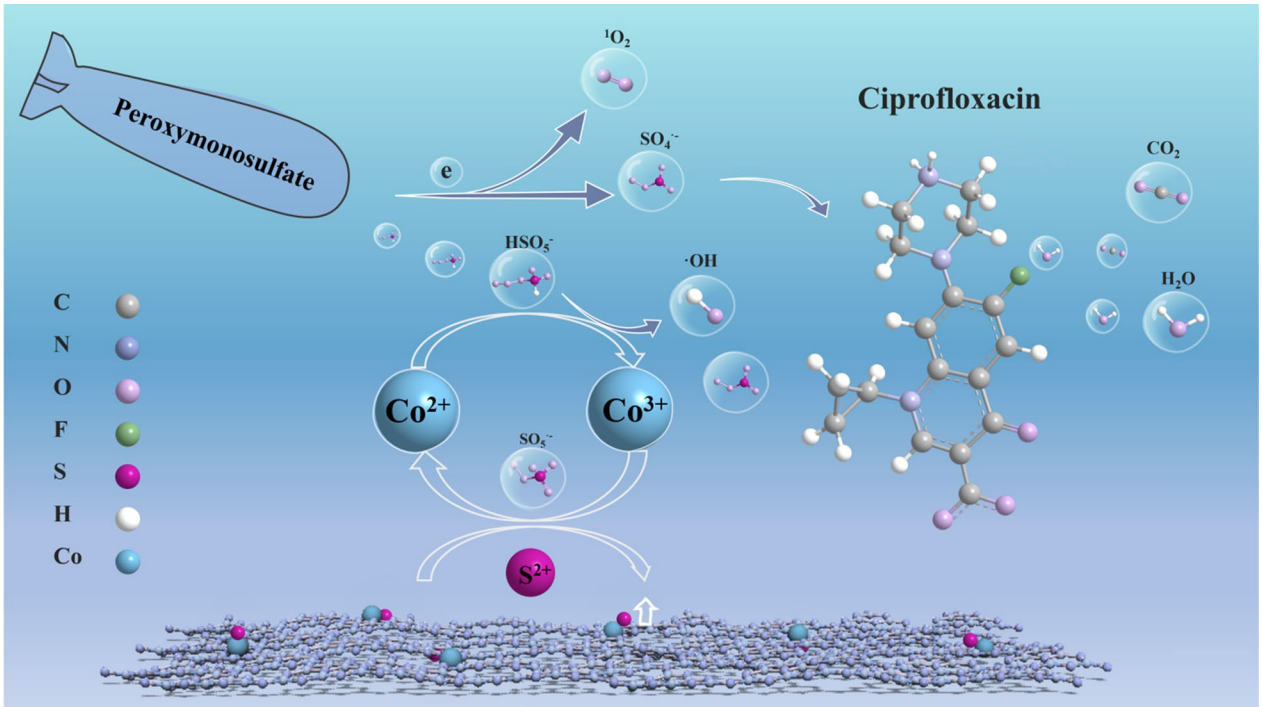

Scheme 2. Possible mechanism of CoS@MLBC/PMS system on CIP degradation

Based on the above-mentioned analysis, the possible mechanism of CIP degradation in the CoS@MLBC/PMS system was as follows (Scheme 2): The O–O bond in PMS was broken by the absorption electrons from CoS@MLBC to generate ·OH and SO_4·$^-$, and Co^{2+} could combine with HSO_5^- to produce ·OH, SO_4·$^-$ and Co^{3+} (Additional file 1: Eqs. S6-7). The generated Co^{3+} could further react with PMS to produce $SO_5$$^-$· (Additional file 1: Eqs. S14), indicating that the Co^{2+}/Co^{3+} cycle significantly contributed to the activation of PMS (Hu and Long 2016). Additionally, $SO_5$$^-$· could self-react or react with H_2O to further generate $^1O_2$ (Additional file 1: Eqs. S15-16). Overall, the CoS@MLBC could efficiently activate PMS to generate ROSs for degradation of CIP.

3.4 Intermediate identification and toxicity prediction

3.4.1 Degradation pathways and intermediate analysis

In the CoS@MLBC/PMS system, twelve significant intermediates generated from the degradation process of CIP were successfully identified using HPLC/MS analysis. Three possible degradation pathways of CIP were initially proposed, and the molecular weights and structures of the intermediates were analyzed in detail (Fig. 7). For Pathway I, the formation of P1 (m/z 362) could be attributed to the cleavage of the piperazine ring, resulting in a dialdehyde derivative structure. Then, P1 lost two formaldehyde groups one after another to form P2 (m/z 334) and P3 (m/z 306). The secondary amine nitrogen lost from P3 was rapidly oxidized, resulting in the formation of P4 (m/z 291), and subsequent loss of formaldehyde from P4 led to the generation of P5 (m/z 263), ultimately leading to complete cleavage of the piperazine ring. Pathway II began with the oxidation of the cyclopropyl group and cleavage to create P6 (m/z 292). Subsequently, the piperazine ring underwent fragmentation, resulting in the generation of P7 (m/z 223). Finally, the elimination of the carboxyl group from the quinolone ring yielded P8 (m/z 179). Pathway III was designated as the defluorination (−OH substitution -F) to form P9 (m/z 330). On this basis, the cleavage and elimination of both the cyclopropyl group and carboxyl group from the quinolone ring by the Kolbe decarboxylation reaction generated P10 (m/z 304), P11 (m/z 177). According to Additional file 1: Fig. S13, the intermediates of Pathway I and Pathway III had higher intensity in the ion chromatogram. They were the primary degradation pathways of the degradation process, while Pathway II was the minor pathway.

3.4.2 Toxicity prediction of CIP and its intermediate

In order to predict and comprehend the potential ecotoxicity of CIP and its degradation products on aquatic organisms during catalyst degradation, we utilized the EPI Suite software to calculate the acute and chronic toxicity levels of CIP and its degradation products on marine organisms across three distinct trophic levels. The toxicity assessment was based on the Chinese hazard evaluation guidelines for new chemical substances (HJ/T 154-2004) and European Union criteria (Additional file 1: Table S3). The acute toxicity of the substance was evaluated by determining LC_{50} values for fish and Daphnia,

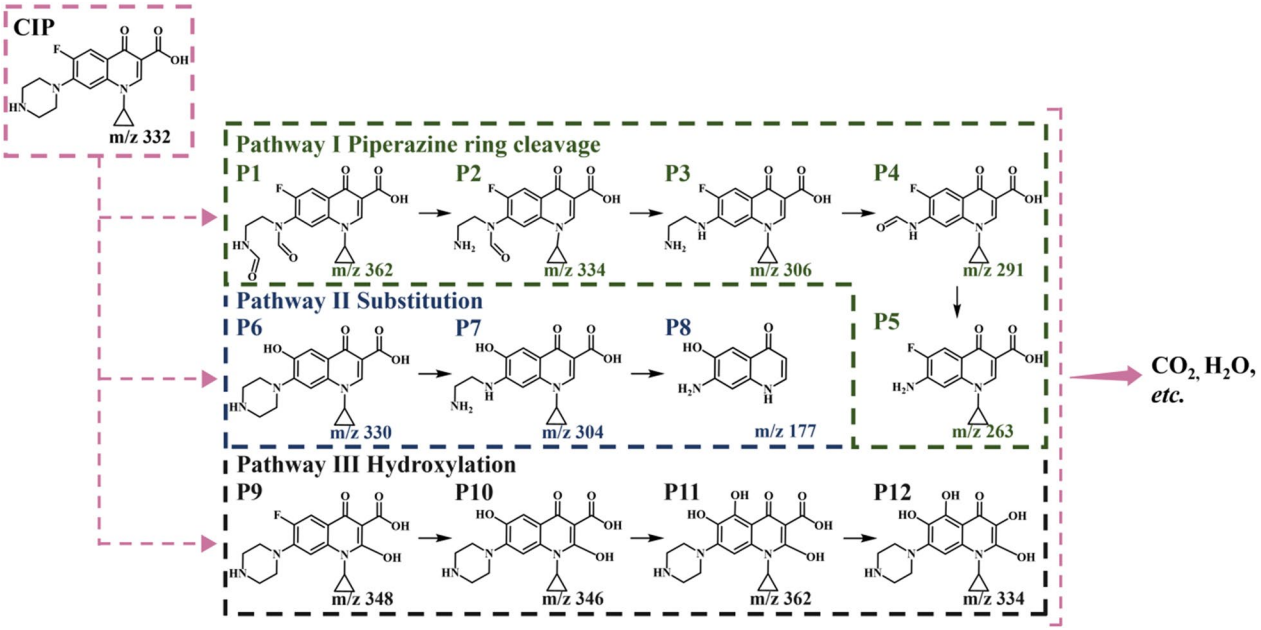

Fig. 7 Possible degradation pathways of CIP in the CoS@MLBC/PMS system

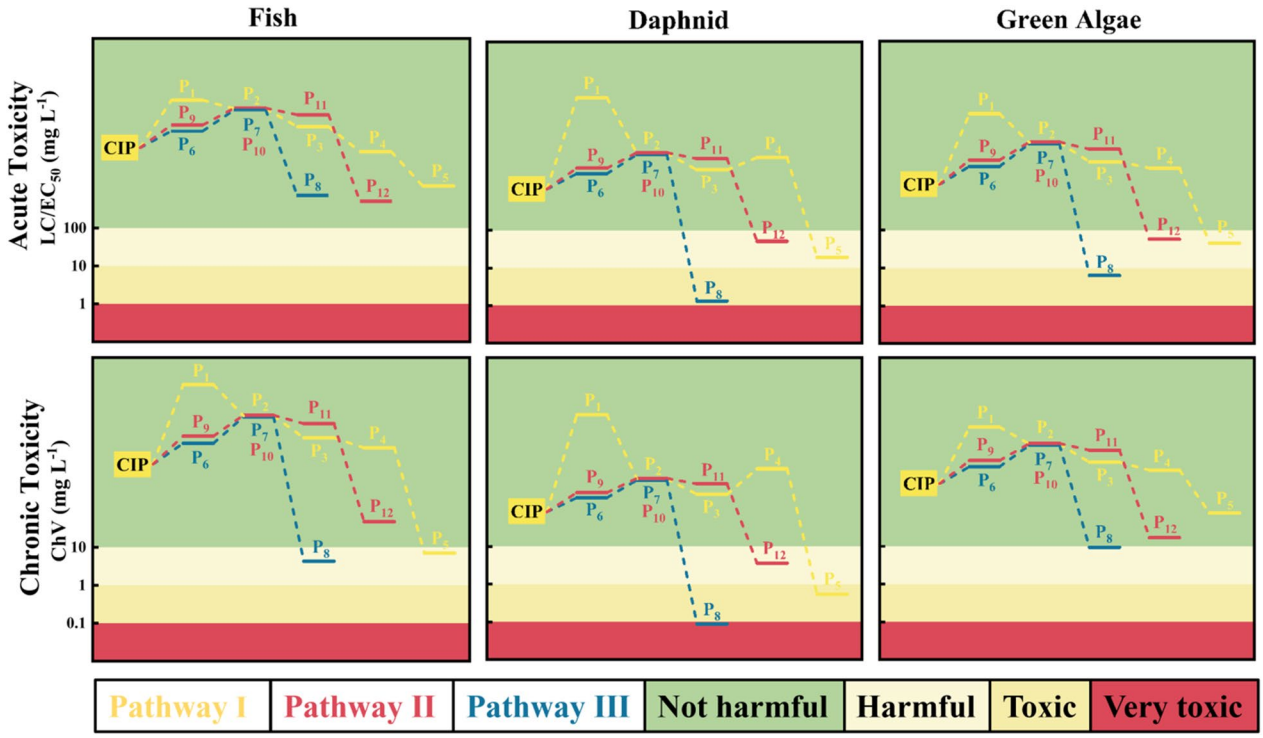

Fig. 8 Evaluation of acute and chronic toxicity of CIP and its degradation intermediates towards three aquatic organisms using EPI Suite software

as well as EC_{50} values for green algae, based on the data presented in Fig. 8 and Additional file 1: Table S4. The results revealed that CIP exhibited no detrimental effects on aquatic organisms. Intermediates with LC/EC_{50} and ChVs higher than 100 and 10 mg L^{-1}, respectively, indicate that the negotiators were non-toxic and harmless to the organism. The mediators of the three pathways exhibited minimal toxicity towards fish, Daphnia, and green algae, except for P5, P8, and P12. It was observed that P5 displayed toxicity towards Daphnia and had detrimental effects on the health of fish and green algae. Similarly, P8 was found to be harmful to fish and green algae while exhibiting toxic effects on Daphnia. Furthermore, although P12 demonstrated adverse effects on Daphnia and green algae, it did not exhibit any detrimental impact on fish. In conclusion, the efficiency of CIP mineralization could be enhanced by extending the reaction duration, thereby mitigating system toxicity, indicating that the catalyst is eco-friendly in the CIP degradation process.

4 Conclusion

In this work, a novel catalyst CoS@MLBC with carbon nitride structure was synthesized by a one-step HTC method using invasive plants as biomass feedstock, which can efficiently activate PMS to degrade CIP in water. Various characterizations and performance analyses revealed the successful synthesis of carbon nitride structures and the good efficiency of CoS@MLBC for the degradation of CIP. Meanwhile, the advantage of invasive plants for Co-modified biochar synthesis was illustrated through comparative analyses with that prepared using common biomass feedstocks (corn cop and wheat straw). The quenching experiments and EPR analysis were utilized to identify the main active species as ·OH, $SO_4^{\cdot-}$ and $^1O_2$ towards CIP degradation. In addition, CoS@MLBC showed good stability and practicality through cycling experiments and actual water testing. Finally, the degradation pathways and intermediates of CIP were analyzed by HPLC–MS, and their ecotoxicity was predicted. In conclusion, this work provides a new perspective on the preparation of biochar from invasive plants for the efficient degradation of antibiotics in water.

Supplementary Information

The online version contains supplementary material available at https://doi.org/10.1007/s42773-024-00325-2.

Additional file 1. Supplementary texts, figures, tables, equations.

Acknowledgements
The authors acknowledge the research facilities of the Chongqing Institute of Green and Intelligent Technology, Chinese Academy of Sciences, and the valuable comments of anonymous reviewers and editors.

Author contributions
Yu-Wei Lu: Conceptualization, Investigation, Visualization, Data curation, Formal analysis, Writing—original draft, Writing—review and editing. Yu-Han Fan: Investigation, Data curation, Validation, Writing—review and editing. Ming Chen: Conceptualization, Funding acquisition, Supervision, Validation. All authors read and approved the final manuscript.

Funding
The study was financially supported by the Major Science and Technology Project from the Ministry of Water Resources (SKS-2022069), Science and Technology Program of Inner Mongolia Autonomous Region (2021GG0089), Postdoctoral Innovative Talent Support Program of Chongqing, China, 2020, and Natural Science Foundation of Chongqing, China (cstc2021jcyj-bshX0104 and cstc2021jcyj-msxmX0163), National Natural Science Foundation of China (22306181).

Availability of data and materials
Authors can confirm that all relevant data are included in the article.

Declarations

Ethics approval and consent to participate
Not applicable.

competing interests
The authors declare that they have no known competing financial interests or personal relationships that could have appeared to influence the work reported in this paper.

Author details
[1]Key Laboratory of Reservoir Aquatic Environment, Chongqing Institute of Green and Intelligent Technology, Chinese Academy of Sciences, Chongqing 400714, China. [2]College of Resources and Environment, Yangtze University, Wuhan 430100, China. [3]Chongqing School, University of Chinese Academy of Sciences, Chongqing 400714, China.

Received: 23 September 2023 Revised: 15 March 2024 Accepted: 15 March 2024
Published online: 01 April 2024

References

Andrew Lin K-Y, Hsu F-K, Lee W-D (2015) Magnetic cobalt-graphene nanocomposite derived from self-assembly of MOFs with graphene oxide as an activator for peroxymonosulfate. J Mater Chem A 3(18):9480–9490. https://doi.org/10.1039/C4TA06516F

Balakrishnan A, Kunnel ES, Sasidharan R, Chinthala M, Kumar A (2023) 3D black G-C_3N_4 isotype heterojunction hydrogels as a sustainable photocatalyst for tetracycline degradation and H_2O_2 production. Chem Eng J 475:146163. https://doi.org/10.1016/j.cej.2023.146163

Bharathi D, Lee J, Albeshr MF, Alrefaei AF, Le TT, Mathimani T (2023) Enhanced photocatalytic degradation of polycyclic aromatic hydrocarbon by graphitic carbonitride-nickel (g–C_3N_4–Ni) nanocomposite. Chemosphere 345:140464. https://doi.org/10.1016/j.chemosphere.2023.140464

Bicalho HA, Rios RDF, Binatti I, Ardisson JD, Howarth AJ, Lago RM, Teixeira APC (2020) Efficient activation of peroxymonosulfate by composites containing iron mining waste and graphitic carbon nitride for the degradation of acetaminophen. J Hazard Mater 400:123310. https://doi.org/10.1016/j.jhazmat.2020.123310

Bopda A, Mafo SG, Ndongmo JN, Kenda GT, Fotsop CG, Kuete IH, Ngakou CS, Tchuifon DR, Tamo AK, Nche GN, Anagho SG (2022) Ferromagnetic biochar prepared from hydrothermally modified calcined mango seeds for fenton-like degradation of indigo carmine. C 8(4):81. https://doi.org/10.3390/c8040081

Byambaa B, Kim E-J, Seid MG, An B-M, Cho J, Aung SL, Song KG (2023) Synthesis of N-doped sludge biochar using the hydrothermal route-enabled carbonization method for the efficient degradation of organic pollutants by peroxymonosulfate activation. Chem Eng J 456:141037. https://doi.org/10.1016/j.cej.2022.141037

Cao J, Yang Z, Xiong W, Zhou Y, Wu Y, Jia M, Sun S, Zhou C, Zhang Y, Zhong R (2020a) Peroxymonosulfate activation of magnetic co nanoparticles relative to an N-doped porous carbon under confinement: boosting stability and performance. Sep Purif Technol 250:117237. https://doi.org/10.1016/j.seppur.2020.117237

Cao J, Sun S, Li X, Yang Z, Xiong W, Wu Y, Jia M, Zhou Y, Zhou C, Zhang Y (2020b) Efficient charge transfer in aluminum-cobalt layered double hydroxide derived from co-zif for enhanced catalytic degradation of tetracycline through peroxymonosulfate activation. Chem Eng J 382(2):122802. https://doi.org/10.1016/j.cej.2019.122802

Chen C-W, Binh NT, Hung C-M, Chen C-F, Dong C-D (2015) Removal of polycyclic aromatic hydrocarbons from sediments using chemical oxidation processes. J Adv Oxid Technol 18(1):15–22. https://doi.org/10.1515/jaots-2015-0102

Chen Z, Li T, Zhu Y, Liang X, Zhao Z, Wang D, Li J, Gao Y, Hu C (2021) Efficient light-free activation of peroxymonosulfate by carbon ring conjugated carbon nitride for elimination of organic pollutants. Chem Eng J 420:129671. https://doi.org/10.1016/j.cej.2021.129671

Essl F, Bacher S, Genovesi P, Hulme PE, Jeschke JM, Katsanevakis S, Kowarik I, Kühn I, Pyšek P, Rabitsch W, Schindler S, Van Kleunen M, Vilà M, Wilson JRU, Richardson DM (2018) Which taxa are alien? Criteria, applications, and uncertainties. Bioscience 68(7):496–509. https://doi.org/10.1093/biosci/biy057

Fan Y-H, Li Y-Q, Hayat F, Liu C, Li J, Chen M (2023a) Multi-targeted removal of coexisted antibiotics in water by the synergies of radical and non-radical pathways in PMS activation. Sep Purif Technol 305:122475. https://doi.org/10.1016/j.seppur.2022.122475

Fan Y-H, Lu Y-W, Hayat F, Mei Y-H, Chen M (2023b) Overcoming slow removal efficiency-induced highly toxic i-dbps in water by oxygen vacancies enriched invasive plant biochar catalyst: experimental and theoretical studies. J Hazard Mater 459:132086. https://doi.org/10.1016/j.jhazmat.2023.132086

Fang Z, Qi J, Xu Y, Liu Y, Qi T, Xing L, Dai Q, Wang L (2022) Promoted generation of singlet oxygen by hollow-shell CoS/g-C_3N_4 catalyst for sulfonamides degradation. Chem Eng J 441:136051. https://doi.org/10.1016/j.cej.2022.136051

Feng Q, Wang B, Chen M, Wu P, Lee X, Xing Y (2021) Invasive plants as potential sustainable feedstocks for biochar production and multiple applications: a review. Resour Conserv Recycl 164:105204. https://doi.org/10.1016/j.resconrec.2020.105204

Hong Y, Peng J, Zhao X, Yan Y, Lai B, Yao G (2019) Efficient degradation of atrazine by CoMgAl layered double oxides catalyzed peroxymonosulfate: optimization, degradation pathways and mechanism. Chem Eng J 370:354–363. https://doi.org/10.1016/j.cej.2019.03.127

Hu P, Long M (2016) Cobalt-catalyzed sulfate radical-based advanced oxidation: a review on heterogeneous catalysts and applications. Appl Catal B 181:103–117. https://doi.org/10.1016/j.apcatb.2015.07.024

Huang W-H, Lee D-J, Huang C (2021) Modification on biochars for applications: a research update. Biores Technol 319:124100. https://doi.org/10.1016/j.biortech.2020.124100

Jiang H, Dai Y (2023) Vitamin C modified crayfish shells biochar efficiently remove tetracycline from water: a good medicine for water restoration. Chemosphere 311:136884. https://doi.org/10.1016/j.chemosphere.2022.136884

Jiang H, Li X, Dai Y (2024) Phosphoric acid activation of cow dung biochar for adsorbing enrofloxacin in water: icing on the cake. Environ Pollut 341:122887. https://doi.org/10.1016/j.envpol.2023.122887

Krysanova K, Krylova A, Zaichenko V (2019) Properties of biochar obtained by hydrothermal carbonization and torrefaction of peat. Fuel 256:115929. https://doi.org/10.1016/j.fuel.2019.115929

Kuan J, Zhang H, Gu H, Zhang Y, Wu H, Mao N (2022) Adsorption-enhanced photocatalytic property of Ag-doped biochar/g-C_3N_4/TiO_2 composite by incorporating cotton-based biochar. Nanotechnology 33(34):345402. https://doi.org/10.1088/1361-6528/ac705e

Lei Y, Guo X, Jiang M, Sun W, He H, Chen Y, Thummavichai K, Ola O, Zhu Y, Wang N (2022) Co-ZIF reinforced cow manure biochar (CMB) as an

effective peroxymonosulfate activator for degradation of carbamazepine. Appl Catal B 319:121932. https://doi.org/10.1016/j.apcatb.2022.121932
Li G, Yang H, An T, Lu Y (2018) Antibiotics elimination and risk reduction at two drinking water treatment plants by using different conventional treatment techniques. Ecotoxicol Environ Saf 158:154–161. https://doi.org/10.1016/j.ecoenv.2018.04.019
Li X, Shi Z, Zhang J, Gan T, Xiao Z (2023) Aqueous Cr (VI) removal performance of an invasive plant-derived biochar modified by Mg/Al-layered double hydroxides. Colloid Interface Sci Commun 53:100700. https://doi.org/10.1016/j.colcom.2023.100700
Li X, Jiang H, Zhu L, Tang J, Liu Z, Dai Y (2024) Adsorption interactions between typical microplastics and enrofloxacin: relevant contributions to the mechanism. Chemosphere 351:141181. https://doi.org/10.1016/j.chemosphere.2024.141181
Liang X, Su Y, Wang X, Liang C, Tang C, Wei J, Liu K, Ma J, Yu F, Li Y (2023a) Insights into the heavy metal adsorption and immobilization mechanisms of CaFe-layered double hydroxide corn straw biochar: synthesis and application in a combined heavy metal-contaminated environment. Chemosphere 313:137467. https://doi.org/10.1016/j.chemosphere.2022.137467
Liang J, Fu L, Gao K, Zhang P, Duan X, Gong X, Cai L (2023b) Accelerated sulfate radical generation from peroxymonosulfate by ZIF-67-derived Co_3O_4 encapsulated in g-C_3N_4: a gift from in Situ growth. Chem Eng J 460:141797. https://doi.org/10.1016/j.cej.2023.141797
Liao W, Zhang X, Shao J, Yang H, Zhang S, Chen H (2022) Simultaneous removal of cadmium and lead by biochar modified with layered double hydroxide. Fuel Process Technol 235:107389. https://doi.org/10.1016/j.fuproc.2022.107389
Liu S, Chen L, Liu T, Cai S, Zou X, Jiang J, Mei Z, Gao Z, Guo H (2021) Rich S vacant G-C_3N_4@$CuIn_5S_8$ hollow heterojunction for highly efficient selective photocatalytic CO_2 reduction. Chem Eng J 424:130325. https://doi.org/10.1016/j.cej.2021.130325
Liu C, He X, Xu Q, Chen M (2023a) A general way to realize the bi-directional promotion effects on the photocatalytic removal of heavy metals and organic pollutants in real water by a novel s-scheme heterojunction: experimental investigations, QSAR and DFT calculations. J Hazard Mater 445:130551. https://doi.org/10.1016/j.jhazmat.2022.130551
Liu X, Shao Z, Wang Y, Liu Y, Wang S, Gao F, Dai Y (2023b) New use for lentinus edodes bran biochar for tetracycline removal. Environ Res 216:114651. https://doi.org/10.1016/j.envres.2022.114651
Liu C, He X, Li J, Ma J, Yue J, Wang Z, Chen M (2024) Selective electrophilic attack towards organic micropollutants with superior fenton-like activity by biochar-supported cobalt single-atom catalyst. J Colloid Interface Sci 657:155–168. https://doi.org/10.1016/j.jcis.2023.11.131
Long X, Yang S, Qiu X, Ding D, Feng C, Chen R, Wang X, Chen N, Lei Q (2021) Heterogeneous activation of peroxymonosulfate for bisphenol a degradation using $CoFe_2O_4$ derived by hybrid cobalt-ion hexacyanoferrate nanoparticles. Chem Eng J 404:127052. https://doi.org/10.1016/j.cej.2020.127052
Long Y, Li S, Su Y, Wang S, Zhao S, Wang S, Zhang Z, Huang W, Liu Y, Zhang Z (2021b) Sulfur-containing iron nanocomposites confined in S/N Co-doped carbon for catalytic peroxymonosulfate oxidation of organic pollutants: low iron leaching, degradation mechanism and intermediates. Chem Eng J 404:126499. https://doi.org/10.1016/j.cej.2020.126499
Mahmoud SA, Mohamed FE, El-Sadek BM, Elsawy MM, Bendary SH (2021) Specific capacitance of CoS encapsulated G-C_3N_4 core shell nanocomposite as extremely efficient counter electrode in quantum dots solar cells. J Solid State Electrochem 25(8–9):2345–2360. https://doi.org/10.1007/s10008-021-04992-0
Mei Q, Sun J, Han D, Wei B, An Z, Wang X, Xie J, Zhan J, He M (2019) Sulfate and hydroxyl radicals-initiated degradation reaction on phenolic contaminants in the aqueous phase: mechanisms, kinetics and toxicity assessment. Chem Eng J 373:668–676. https://doi.org/10.1016/j.cej.2019.05.095
Nguyen TB, Huang CP, Doong R, Chen C-W, Dong C-D (2021) CoO-3D ordered mesoporous carbon nitride (CoO@mpgCN) composite as peroxymonosulfate activator for the degradation of sulfamethoxazole in water. J Hazard Mater 401:123326. https://doi.org/10.1016/j.jhazmat.2020.123326
Nguyen T-B, Le V-R, Huang CP, Chen C-W, Chen L, Dong C-D (2022) Construction of ternary $NiCo_2O_4$/MnOOH/GO composite for peroxymonosulfate activation with enhanced catalytic activity toward ciprofloxacin degradation. Chem Eng J 446:137326. https://doi.org/10.1016/j.cej.2022.137326
Nguyen TAH, Bui TH, Guo WS, Ngo HH (2023) Valorization of the aqueous phase from hydrothermal carbonization of different feedstocks: challenges and perspectives. Chem Eng J 472:144802. https://doi.org/10.1016/j.cej.2023.144802
Peng L, Shang Y, Gao B, Xu X (2021) Co_3O_4 anchored in N, S heteroatom co-doped porous carbons for degradation of organic contaminant: role of pyridinic N-Co binding and high tolerance of chloride. Appl Catal B 282:119484. https://doi.org/10.1016/j.apcatb.2020.119484
Pyšek P, Richardson DM (2010) Invasive species, environmental change and management, and health. Annu Rev Environ Resour 35(1):25–55. https://doi.org/10.1146/annurev-environ-033009-095548
Pyšek P, Richardson DM, Rejmánek M, Webster GL, Williamson M, Kirschner J (2004) Alien plants in checklists and floras: towards better communication between taxonomists and ecologists. Taxon 53(1):131–143. https://doi.org/10.2307/4135498
Pyšek P, Hulme PE, Simberloff D, Bacher S, Blackburn TM, Carlton JT, Dawson W, Essl F, Foxcroft LC, Genovesi P, Jeschke JM, Kühn I, Liebhold AM, Mandrak NE, Meyerson LA, Pauchard A, Pergl J, Roy HE, Seebens H, Van Kleunen M, Vilà M, Wingfield MJ, Richardson DM (2020) Scientists' warning on invasive alien species. Biol Rev 95(6):1511–1534. https://doi.org/10.1111/brv.12627
Qiu J, Wang D, Chang Y, Feng Q, Liu Z, Pang M, Meng D, Feng Y, Fan C (2024) Anchoring single-atom Cu on tubular g-C3N4 with defect engineering for enhanced fenton-like reactions to efficiently degrade carbamazepine: performance and mechanism. Chem Eng J 479:147841. https://doi.org/10.1016/j.cej.2023.147841
Ren W, Xiong L, Yuan X, Yu Z, Zhang H, Duan X, Wang S (2019) Activation of peroxydisulfate on carbon nanotubes: electron-transfer mechanism. Environ Sci Technol 53(24):14595–14603. https://doi.org/10.1021/acs.est.9b05475
Ren S, Wang S, Liu Y, Wang Y, Gao F, Dai Y (2023) A review on current pollution and removal methods of tetracycline in soil. Sep Sci Technol 58(14):2578–2602. https://doi.org/10.1080/01496395.2023.2259079
Rodriguez-Narvaez OM, Peralta-Hernandez JM, Goonetilleke A, Bandala ER (2017) Treatment technologies for emerging contaminants in water: a review. Chem Eng J 323:361–380. https://doi.org/10.1016/j.cej.2017.04.106
Sengottian M, Venkatachalam CD, Ravichandran SR (2022) Optimization of alkali catalyzed hydrothermal carbonization of prosopis juliflora woody biomass to biochar for copper and zinc adsorption and its application in supercapacitor. Int J Electrochem Sci 17(9):220938. https://doi.org/10.20964/2022.09.22
Shaheen N, Waqas M, Alazmi A, Alkhudhayri AA, Hasan M, Shahid M, Warsi MF, Alsafari IA (2022) Hydrothermal assisted WO_3@C nanowires supported G-C_3N_4 ternary nanocomposites for the removal of colored and colorless organic effluents and bacterial strains. Mater Chem Phys 292:126754. https://doi.org/10.1016/j.matchemphys.2022.126754
Shang Y, Chen C, Zhang P, Yue Q, Li Y, Gao B, Xu X (2019) Removal of sulfamethoxazole from water via activation of persulfate by Fe_3C@NCNTs including mechanism of radical and nonradical process. Chem Eng J 375:122004. https://doi.org/10.1016/j.cej.2019.122004
Sun H, Xie G, He D, Zhang L (2020) Ascorbic acid promoted magnetite fenton degradation of alachlor: mechanistic insights and kinetic modeling. Appl Catal B 267:118383. https://doi.org/10.1016/j.apcatb.2019.118383
Sun D, Lv Z-W, Rao J, Tian R, Sun S-N, Peng F (2022) Effects of hydrothermal pretreatment on the dissolution and structural evolution of hemicelluloses and lignin: a review. Carbohyd Polym 281:119050. https://doi.org/10.1016/j.carbpol.2021.119050
Tan H, Gu X, Kong P, Lian Z, Li B, Zheng Z (2019) Cyano group modified carbon nitride with enhanced photoactivity for selective oxidation of benzylamine. Appl Catal B 242:67–75. https://doi.org/10.1016/j.apcatb.2018.09.084
Wang Y, Zhang Y, Zhao S, Huang Z, Chen W, Zhou Y, Lv X, Yuan S (2019) Biotemplate synthesis of mo-doped polymer carbon nitride for photocatalytic hydrogen evolution. Appl Catal B 248:44–53. https://doi.org/10.1016/j.apcatb.2019.02.007
Wang Q, Xu Z, Wang S, Wang Z, Jia J, Li H, Cao Y, Chen Y, Qin Y, Cui F (2021) Rapid synthesis of amorphous coo nanosheets: highly efficient catalyst for parachlorophenol degradation by peroxymonosulfate activation. Sep Purif Technol 263:118369. https://doi.org/10.1016/j.seppur.2021.118369

Wang Y, Ma J, Yang L, Li Y, Chen M (2023a) Removal of antibiotic resistant bacteria and genes by post-pyrolysis bio-hybridcarbon/peroxymonosulfate system: gene-degrading intermediates of bioinformatic identification based on corrected-nanopore sequencing and preference mechanism. Chem Eng J 460:141809. https://doi.org/10.1016/j.cej.2023.141809

Wang J, Lu X, Jing Q, Zhang B, Ye J, Zhang H, Xiao Z, Zhang J (2023b) Spatiotemporal characterization of heavy metal and antibiotics in the Pearl river basin and pollutants removal assessment using invasive species-derived biochars. J Hazard Mater 454:131409. https://doi.org/10.1016/j.jhazmat.2023.131409

Wen J, Sun S, Tang Q, Song C, Wang J, Zhang W, Zhou L, Gao Y, Xiao X (2023) Inactivation of microcystis aeruginosa under visible light by Bi_5O_7I/g-C_3N_4 photocatalyst: performance and optimization. Chem Eng J 475:146526. https://doi.org/10.1016/j.cej.2023.146526

Yang Z, Wang Z, Liang G, Zhang X, Xie X (2021) Catalyst bridging-mediated electron transfer for nonradical degradation of bisphenol a via natural manganese ore-cornstalk biochar composite activated peroxymonosulfate. Chem Eng J 426:131777. https://doi.org/10.1016/j.cej.2021.131777

Yu G, Gong K, Xing C, Hu L, Huang H, Gao L, Wang D, Li X (2023) Dual P-doped-site modified porous g-C_3N_4 achieves high dissociation and mobility efficiency for photocatalytic H_2O_2 production. Chem Eng J 461:142140. https://doi.org/10.1016/j.cej.2023.142140

Yuan R, Qiu J, Yue C, Shen C, Li D, Zhu C, Liu F, Li A (2020) Self-assembled hierarchical and bifunctional MIL-88A(Fe)@$ZnIn_2S_4$ heterostructure as a reusable sunlight-driven photocatalyst for highly efficient water purification. Chem Eng J 401:126020. https://doi.org/10.1016/j.cej.2020.126020

Zhang Z, Chen L, Wang J, Yao J, Li J (2018) Biochar preparation from solidago canadensis and its alleviation of the inhibition of tomato seed germination by allelochemicals. RSC Adv 8(40):22370–22375. https://doi.org/10.1039/C8RA03284J

Zhang W, Li G, Liu H, Chen J, Ma S, Wen M, Kong J, An T (2020) Photocatalytic degradation mechanism of gaseous styrene over Au/TiO_2@CNTs: relevance of superficial state with deactivation mechanism. Appl Catal B 272:118969. https://doi.org/10.1016/j.apcatb.2020.118969

Zhao G, Li W, Zhang H, Wang W, Ren Y (2022) Single atom Fe-dispersed graphitic carbon nitride (g-C_3N_4) as a highly efficient peroxymonosulfate photocatalytic activator for sulfamethoxazole degradation. Chem Eng J 430:132937. https://doi.org/10.1016/j.cej.2021.132937

Zhou Y, Shen C, Xiang L, Xue Y, Lu M, Wang T (2023) Facile synthesis of magnetic biochar from an invasive aquatic plant and basic oxygen furnace slag for removal of phosphate from aqueous solution. Biomass Bioenerg 173:106800. https://doi.org/10.1016/j.biombioe.2023.106800